Targeted Photothermal Ablation of Murine Melanomas with Melanocyte-Stimulating Hormone Analog-Conjugated Hollow Gold Nanospheres

Wei Lu[1], **Chiyi Xiong**[1], **Guodong Zhang**[1], **Qian Huang**[1], **Rui Zhang**[1], **Jin Z. Zhang**[2], and **Chun Li**[1],*

[1] Department of Experimental Diagnostic Imaging, The University of Texas M. D., Anderson Cancer Center, Houston, Texas 77030

[2] Department of Chemistry and Biochemistry, University of California, Santa Cruz, California 95064

Abstract

Purpose—To develop melanoma-targeted hollow gold nanospheres (HAuNS) and evaluate their potential utility for selective photothermal ablation (PTA) in melanoma.

Experimental Design—A new class of photothermal coupling agents based on HAuNS was synthesized. HAuNS were stabilized with poly(ethylene-glycol) coating and attached with α-melanocyte-stimulating hormone analog, [Nle^4,D-Phe^7]α-MSH (NDP-MSH), which is a potent agonist of melanocortin type-1 receptor overexpressed in melanoma. The intracellular uptake of the NDP-MSH-conjugated PEGylated HAuNS (NDP-MSH-PEG-HAuNS) and the distribution of β-arrestin were examined in murine B16/F10 melanoma cells. The biodistribution of NDP-MSH-PEG-HAuNs was assessed at 4 h post intravenous injection in tumor-bearing nude mice. PTA effect of the nanoparticles was evaluated both histologically using excised tissue and functionally by [^{18}F] fluorodeoxyglucose positron emission tomography ([^{18}F]FDG-PET).

Results—NDP-MSH-PEG-HAuNS consist only of a thin gold wall with hollow interior (outer diameter, 43.5±2.3 nm; shell thickness, 3–4 nm), which display strong and tunable resonance absorption in near-infrared region (NIR, peak 808 nm). The nanoparticles were specifically taken up by melanoma cells, which initiated the recruitment of β-arrestins, the adapters to link the activated G-protein-coupled receptors to clathrin, indicating the involvement of receptor-mediated endocytosis. This resulted in enhanced extravasation of NDP-MSH-PEG-HAuNS from tumor blood vessels and their dispersion into tumor matrix compared with non-specific PEGylated HAuNS. Successful selective PTA of B16/F10 melanoma with targeted HAuNS was confirmed by histological and [^{18}F]FDG-PET evaluation at 24 h post NIR laser irradiation at a low dose energy of 30 J/cm^2.

*Corresponding author: Department of Experimental Diagnostic Imaging, Unit 59, The University of Texas M. D. Anderson Cancer Center, 1515 Holcombe Boulevard, Houston, Texas 77030. Phone: (713) 792-5182. Fax: (713) 794-5456., e-mail: cli@di.mdacc.tmc.edu.

Statement of Translational Relevance: We report a new melanoma-targeted photothermal coupling agents based on hollow gold nanospheres. The combination of spherical shape, small size (average diameter ~40 nm), absence of silica core, and tunable and strong absorption bands in near infrared region makes these nanoparticles ideally suited for photothermal ablation applications. By using peptides as the targeting ligand, we demonstrated receptor-mediated active targeting and efficient photothermal ablation of melanoma in a murine tumor model. The newly developed nanoparticles are particularly relevant to clinical translation for photothermal ablation of melanoma because these lesions are accessible to near-infrared light penetration. Targeted delivery of nanoparticles to melanoma could increase the efficacy, decrease the energy dose of the laser, and minimize the potential for damage to surrounding normal tissues. In addition, noninvasive [^{18}F]FDG PET can be useful in monitoring early treatment response after photothermal ablation, which can have significant implication in the clinic in guiding repeat ablation procedures.

Conclusion—NDP-MSH-PEG-HAuNS have the potentials to mediate targeted photothermal ablation of melanoma.

Keywords

hollow gold nanospheres; melanocyte-stimulating hormone; photothermal ablation; melanoma; targeting

1. Introduction

Malignant melanoma is one of the most lethal cancers. Its incidence is increasing rapidly, making it a significant public health problem (1). Although the disease is considered to be highly treatable upon early diagnosis, the prognosis upon onset of metastasis is dire, typified by a 13% of 5-year survival rate once distant malignancy has occurred (2). Besides surgery, radiation therapy, and chemotherapy, other novel strategies including photothermal sensitization and photothermal ablation (PTA) therapy with near infrared (NIR) laser light have been explored for the treatment of melanoma (2–6). Here, the development of novel photothermal coupling agents will be necessary for increasing the PTA efficiency, decreasing the energy dose of the laser light, and minimizing the potential for damage to surrounding normal tissues.

Nanostructures of noble metals such as gold can exhibit a strong optical extinction at NIR wavelengths (700–850 nm), where optical absorption in tissue is minimal and penetration is optimal (7–13). The efficiency of PTA can be significantly enhanced by integrating the light-absorbing material into the target tissue to mediate selective photothermal effects. Several studies have explored the use of gold nanostructures for cancer PTA, including nanorods (11), nanocages (10), and "core/shell" structures (7–9,12,13). However, a major and challenging requirement for successful biomedical applications of nanomaterials is efficient *in vivo* delivery to the target sites after systemic administration (14,15).

Recently, a second generation nanostructure based on hollow gold nanopsheres (HAuNS) has been fabricated (16). These gold nanostructures have the unique combination of small size (outer diameter, 30–60 nm), spherical shape, hollow interior, and strong and tunable (520 – 950 nm) absorption band as a result of their highly uniform structure (16,17). When coated with polyethylene glycol (PEG), HAuNS with diameter in the sub-nanometer range (<100 nm) display prolonged blood circulation half-life (18,19). By enhanced permeability and retention (EPR) effect (20), the long circulating HAuNS may have a better chance of reaching the tumors through leaky tumor vasculature. Since the passive diffusion of the nanoparticle to tumors is dominated by the pore cut-off size of the tumor blood vessels, the smaller HAuNS as compared to larger silica-cored nanoshells have the obvious advantage in crossing the tumor vessel wall (7,9). This is particularly true for such tumors as glioma and ovarian cancer that have small pore cutoff size of 7–100 nm (21,22).

In the present work, we describe a new class of active targeting photothermal coupling agents which combined the HAuNS with a small-molecular-weight peptide, [Nle^4,D-Phe^7]α-MSH (NDP-MSH) as a targeting moiety. NDP-MSH is a potent agonist of melanocortin type-1 receptor (MC1R) overexpressed in many melanoma cells (23–25), and binds to MC1R with high affinity (IC$_{50}$ = 0.21 nM) (26,27). We hypothesized that targeted delivery of NDP-MSH-conjugated PEGylated HAuNS (NDP-MSH-PEG-HAuNS) to melanoma following intravenous administration could increase the efficiency of PTA with NIR laser. Towards this end, we investigated the intracellular and tissue distribution of the NDP-MSH-PEG-HAuNS. Furthermore, the efficacy of selective PTA with NDP-MSH-PEG-HAuNS against both murine B16/F10 melanoma cells *in vitro* and B16/F10 tumors in nude mice *in vivo* was evaluated. Our

results confirmed successfully active targeting of NDP-MSH-PEG-HAuNS to melanoma and suggested its potential application in targeted PTA therapy of melanoma.

2. Materials and Methods

Materials

All N^α-9-fluorenylmethyloxycarbonyl (Fmoc) amino acids, 2(1H-benzotriazole-1-yl)1,1,3,3-tetramethyluronium hexafluorophosphate (HBTU), 1-hydroxybenzotriazole (HOBt), N',N'-disuccinimidyl carbonate, diisopropylethylamine, and Rink amide resin (4-(2′,4′-dimethoxyphenyl-Fmoc-aminomethyl)phenoxy resin were purchased from Nova-Biochem (San Diego, CA). The following side chain protecting groups were used: 1-(4,4-dimethyl-2,6-dioxocyclohex-1-ylidene)ethyl (Dde) for Lys [Lys(N^ε-Dde)], t-butoxycarbonyl (Boc) for Trp [Trp(N^{in}-Boc)], 2,2,4,6,7-pentamethyldihydro-benzofuran-5-sulfonyl (Pbf) for Arg [Arg(N-Pbf)], trityl (Trt) for His [His(N^{im}-Trt)], and t-butyl (tBu) for Glu [Glu(tBu)], Ser [Ser(tBu)], and Tyr [Tyr(tBu)]. Trifluoroacetic acid, triethylsilane, and piperidine were purchased from Chem-Impex International (Wood Dale, IL). Methoxy-polyethylene glycol-SH (PEG-SH, molecular weight, 5,000) was purchased from Nektar (Huntsville, AL). NH_2-PEG-COOH HCl (MW 5,000) was purchased from JenKem Technology (Allen, TX). Cobalt chloride hexahydrate, sodium borohydride, chloroauric acid trihydrate, hydroxylamine, and dialysis bag (molecular weight cut-off, 1,000) were purchased from Fisher Scientific (Waltham, MA). N-succinimidyl S-acetylthioacetate (SATA), hydrazine, 4′,6-diamidino-2-phenylindole (DAPI), N-(2-(2-(2-Aminoethoxy)ethoxy)ethyl)-lipoic acid, fluorescein isothiocyanate (FITC), dimethylformamide (DMF), and all the other solvents were purchased from Sigma-Aldrich Chemical (St. Louis, MO). PD-10 columns were purchased from Amersham-Pharmacia Biotech (Piscataway, NJ). All the chemicals and solvents were at least ACS grade and were used without further purification.

Conjugation of PEG and NDP-MSH to HAuNS

HAuNS were synthesized according to Schwartzberg et al. (16) with some modifications (see Supplementary Information). Lys^{11}-ε-NH_2-protected NDP-MSH peptide, Ser-Tyr-Ser-Nle-Glu-His-d-Phe-Arg-Trp-Gly-Lys(Dde)-Pro-Val-NH_2 {[Lys^{11}(Dde)]NDP-MSH}, was synthesized manually using Rink amide resin and N^α-Fmoc chemistry. The peptide was conjugated to one terminus of a heterodifunctional PEG precursor, N-hydroxysuccinimidyl-PEG-S-acetylthioacetate (NHS-PEG-SATA; molecular weight, 5000), through its N-terminal amine and activated ester in NHS-PEG-SATA. After removal of the protection group Dde in [Lys^{11}(Dde)]NDP-MSH with 2% hydrazine in DMF, the sulfohydryl group on the other terminus of NDP-MSH-PEG-SATA was released by treatment with 0.5 M hydroxylamine in PBS (Fig. S1). [Lys^{11}(Dde)]NDP-MSH and NDP-MSH-PEG-SH were validated by liquid chromatography-mass spectrometry on an Agilent 1100 Series LC/MSD-TOF instrument (Santa Clara, CA) equipped with a Vydac C18 column (4.6×250 mm, 7 μm, 300 Å). For conjugation of NDP-MSH-PEG-SH, HAuNS (8.5×10^{12} particles/mL) was added to argon-purged aqueous solution containing NDP-MSH-PEG-SH (50 μg/mL) and PEG-SH (500 μg/mL). The reaction was allowed to proceed overnight at room temperature. For purification, the reaction mixture was centrifuged at 7000 rpm for 15 min, and the resulting pellet was resuspended with deionized water. The process was repeated twice to remove unreacted PEG molecules. PEG-SH was conjugated to HAuNS similarly to give PEG-HAuNS, which served as a nonspecific control.

Tagging HAuNS with FITC

In our preliminary studies, we found that although HAuNS could be readily visualized by acquiring their light-scattering signal using a microscope equipped with a darkfield condenser, the scattered light from melanin pigment in B16/F10 cells interfered with unambiguous

identification of HAuNS. Therefore, we introduced a fluorescent dye to HAuNS through lipoic acid (Fig. S2). Briefly, FITC (197 mg, 0.51 mmol) was first conjugated to *N*-(2-(2-(2-aminoethoxy)ethoxy)ethyl)-lipoic acid (116 mg, 0.34 mmol) in 2 mL of anhydrous DMF in the presence of diisopropylethylamine (0.57 mL). After removal of the solvent under reduced pressure, the crude product was purified using silica gel chromatography to yield *N*-(2-(2-(2-(3-fluoresceinthioureido)ethoxy)ethoxy)ethyl)-lipoic acid (FITC-lipoic acid) (125 mg, 51.0%). For FITC labeling of nanoparticles, FITC-lipoic acid (50 μg/mL, 1 mL) was mixed with 9 mL aqueous solution of HAuNS (8.5×10^{12} particles/mL) in the presence of NDP-MSH-PEG-SH (50 μg/mL) and PEG-SH (500 μg/mL) or PEG-SH alone (500 μg/mL). The products were purified by centrifugation and resuspension steps as described in the preceding section.

Characterization of HAuNS

For transmission electron microscopy (TEM), aqueous solution of HAuNS was deposited on copper grid without negative staining. The nanoparticles were allowed to adhere on the grid for 1 h, after which they were briefly rinsed with deionized water and air dried. The samples were then examined using a transmission electron microscope (JEM 1010, JEOL USA, Peabody, MA) at an accelerating voltage of 80 kV. Digital images were obtained using the AMT Imaging System (Advanced Microscopy Techniques Corp, Danvers, MA). The average diameter of HAuNS and thickness of the shell were determined by measuring up to 45 individual particles.

The UV-Vis spectroscopy of HAuNS was recorded on a Beckman Coulter DU-800 UV-Vis spectrometer (Fullerton, CA) with a 1.0-cm optical path length quartz cuvette. The concentration of gold atoms of a HAuNS solution was analyzed by inductively coupled plasma mass spectroscopy (Galbraith, Knoxville, TN). The stability of HAuNS in PBS and serum was investigated by incubating HAuNS in PBS, PBS containing 10% goat serum, or full goat serum at 37°C for up to 24 h. The formation of aggregates over time was observed visually.

Immunogold staining

About 1.0×10^{12} NDP-MSH-PEG-HAuNS or PEG-HAuNS were incubated with rabbit anti-α-MSH polyclonal antibodies (1:100, ICN Biomedicals, Inc., Aurora, OH) in 1 mL of PBS containing 1% bovine serum albumin and 10% glycerol at 37°C for 1 h. The particles were passed through a Sepharose CL-4B column (Sigma, Saint Louis, MO) to separate unstained antibody. The antibody-stained HAuNS were further incubated with 5-nm colloid gold-conjugated goat anti-rabbit immunoglobulin G (IgG) (1:100, Sigma) at 37°C for 1 h. HAuNS were directly visualized using TEM (JEM 1010 microscope; JEOL USA, Peabody, MA) at an accelerating voltage of 80 kV. NDP-MSH-PEG-HAuNS incubated with colloid gold-conjugated goat anti-rabbit IgG without prior treatment with anti-α-MSH were used as a negative control.

Cell uptake and trafficking

B16/F10 cells (American Type Culture Collection, 5000 per well) were seeded in a 96-well plate 1 day before the experiment. The cells were then incubated with FITC-tagged NDP-MSH-PEG-HAuNS or FITC-tagged PEG-HAuNS in RPMI-1640 without phenol red ($\sim 3 \times 10^{11}$/mL) at 37°C for 1 h, followed by fixation in 4% paraformaldehyde. For inhibition study, the cells were incubated with free NDP-MSH (200 μg/mL) for 30 min before addition of FITC-tagged NDP-MSH-PEG-HAuNS. After washing and fixation, cell nuclei were stained with DAPI. To evaluate β-arrestin activation and recruitment, cells were treated with FITC-tagged NDP-MSH-PEG-HAuNS or PEG-HAuNS for 15 min and then subjected to β-arrestin immunohistostaining with goat anti-β-arrestin-2 polyclonal antibodies and donkey anti-goat IgG tetramethyl rhodamine isothiocyanate conjugate (both from Santa Cruz Biotechnology, Inc., Santa Cruz, CA). The cellular fluorescence was examined under a Zeiss Axio Observer.Z1 fluorescence

microscope (Carl Zeiss MicroImaging GmbH, Göttingen, Germany). For TEM, the cellular uptake study was performed in a 24-well plate for 15 min at 37°C. The cells were fixed with a cocktail containing 2% paraformaldehyde and 3% glutaraldehyde, and samples were prepared using standard procedures for biological samples.

In vitro PTA of melanoma cells

B16/F10 cells were seeded onto a 96-well plate at a density of 10,000/well 1 day before the irradiation experiment. Cells were washed three times with RPMI-1640 without phenol red. The following treatments were used: NDP-MSH-PEG-HAuNS plus NIR laser, PEG-HAuNS plus NIR laser, NIR laser alone, and NDP-MSH-PEG-HAuNS alone. For treatments, cells were incubated with NDP-MSH-PEG-HAuNS or PEG-HAuNS (100 μL, 3×10^{11}/ml) at 37°C for 1 h. Thereafter, cells were washed three times with PBS to remove unbound HAuNS. Cells were then re-supplied with RPMI-1640 containing 10% fetal bovine serum. Cells were irradiated with NIR laser light centered at 808 nm at an output power of 32 W/cm^2 for 3 min (15PLUS laser, Diomed, Andover, MA) and then incubated at 37°C for 24 h. The diode laser was coupled to a 1-m, 2-mm core fiber, which delivered a circular laser beam of 2 mm in diameter, covering the central area of the microplate well. Power calibration was performed automatically.

Twenty-four hours after laser treatment, cells were washed three times with Hank's balanced salt solution and stained with calcein AM (Invitrogen, Eugene, OR) for visualization of live cells and with ethidium homodimer (EthD-1, Invitrogen) for visualization of dead cells. Cells were examined using an Olympus Fluoview FV1000 confocal laser scanning microscope (FV1-ASW, Melville, NY) equipped with filter sets specific for excitation/emission wavelengths at 494/517 nm for calcein and 528/617 nm for EthD-1.

Biodistribution-Counting Fluorescent HAuNS Clusters

All experiments involving animals were performed in accordance with the guidelines of the Institutional Animal Care and Use Committee. Nude mice were inoculated subcutaneously with B16/F10 murine melanoma cells (5×10^5) in one flank of the abdomen. When tumors had grown to 4–6 mm in average diameter, the mice were randomly allocated into two groups (n = 5). Each group of mice received an intravenous injection of 2.5×10^{12} NDP-MSH-PEG-HAuNS or PEG-HAuNS. Mice were killed 4 h after injection. Tumor, liver, spleen, kidney, lung, heart, and brain were removed and cryosectioned into 5-μm slices. The sections were stained with the following markers: rabbit anti-mouse MC1R polyclonal antibodies (Millipore, Billerica, MA), rat anti-mouse CD31 monoclonal antibody (Millipore), and/or rabbit anti-CD 68 polyclonal antibodies (Santa Cruz Biotechnology). The secondary antibodies were Alexa Fluor 647-conjugated goat anti-rabbit IgG and Alexa Fluor 594-conjugated goat anti-rat IgG (Invitrogen). Cell nuclei were counterstained with DAPI. The slices were examined under a Zeiss fluorescence microscope equipped with an Apotome module. For quantification of the HAuNS, green fluorescent spots representing nanoparticle aggregates were counted in five randomly selected 0.0358-mm^2 fields per slice at ×200 magnification. The tissue distribution of the HAuNS was calculated as the sum of the green spots in these five fields divided by 0.179 mm^2. Tissue sections from five mice per group were examined. Values are presented as mean ± SD.

Radiolabeling

A chelation agent, *S*-2-(4-[5-{1,2}Dithiolane-3-pentanamide]benzyl)diethylenetriamine pentaacetic acid (DTPA-TA) was synthesized and attached to the surface of HAuNS (See Supplementary Information). For conjugation of radiometal chelator to nanoparticles, DTPA-TA (1 mg/mL, 10 μL) was mixed with 1 mL aqueous solution of HAuNS (1×10^{13} particles/ mL) for 4 h at room temperature. This was followed by conjugation of NDP-MSH-PEG-SH

and PEG-SH to the nanoparticles according to previously described procedures. For radiolabeling, aliquots of NDP-MSH-PEG-HAuNS(DTPA) or PEG-HAuNS(DTPA) (1×10^{13} particles/mL, 0.5 mL) in 0.1 M sodium acetate solution (pH 5.5) were mixed with an aqueous solution of $^{111}InCl_3$ (~200 µCi) for 30 min. The radiolabeled HAuNS was then purified by centrifugation at 8,000 rpm for 5 min and washed three times with PBS. The radiolabeling efficiency and the stability of labeled nanoparticles were analyzed using instant thin layer chromatography (ITLC, See Supplementary Information).

Biodistribution-Radioactivity Counting

Mice bearing s.c. B16/F10 melanoma were randomly allocated into two groups (n = 5). Mice in group 1 were injected with ^{111}In-labeled NDP-MSH-PEG-HAuNS [NDP-MSH-PEG-HAuNS(^{111}In-DTPA)], and mice in group 2 were injected with ^{111}In-labeled PEG-HAuNS [PEG-HAuNS(^{111}In-DTPA)], both at a dose of 2×10^{12} particles/mouse (40 µCi/mouse in 0.2 mL). Mice were killed by CO_2 overexposure 4 h after injection. Blood, heart, liver, spleen, kidney, lung, and tumor tissues were removed and weighed, and radioactivity was measured with a Cobra gamma counter (Packard, Downers Grove, IL). Uptakes of ^{111}In-labeled nanoparticles in various organs were calculated as %ID/g.

In vivo PTA and [^{18}F]fluorodeoxyglucose ([^{18}F]FDG) positron emission tomography (PET)

Nude mice were inoculated subcutaneously with B16/F10 cells in both flanks of the abdomen. The mice were injected intravenously with [^{18}F]FDG (200 µCi, 0.2 mL) before laser treatment. The animals were anesthetized with 2% isofluorane (Baxter, Deerfield, IL), and PET images were acquired 30 min after radiotracer injection using a Rodent R4 microPET scanner (Concorde Microsystems, Inc., Knoxville, TN). The mice were then randomly divided into three groups (n = 3). Mice in each group received an intravenous injection of NDP-PEG-HAuNS (2.5×10^{12} particles/mouse), PEG-HAuNS (2.5×10^{12} particles/mouse), or saline control. Four hours later, the tumor on one flank of each mouse was randomly selected for laser irradiation (808 nm, 0.5 W/cm^2, 1 min). A 5-m, 600-µm core LCM-002 laser collimating fiber (BioTex Inc., Houston, TX) was used to transfer laser power from the laser unit to the target; this delivered a circular laser beam of 1 cm in diameter, covering the surface area of the tumor. Twenty-four hours after laser treatment, the mice again received an intravenous injection of [^{18}F]FDG, and PET images were acquired as above. After the experiments, the mice were killed, and the tumors were removed and weighed. PET images were reconstructed using ASIPro VM 6.3.3.0 software provided by Concorde Microsystems, Inc. (Knoxville, TN). Counts per pixel per minute in the regions of interest were converted to microcuries using a calibration curve derived from scanning standard activity phantoms in the microPET scanner. [^{18}F]FDG uptake in each tumor was divided by the weight of the tumor to obtain percentage of injected dose per gram of tissue (%ID/g).

For histological evaluation, 15 additional tumor-bearing mice were randomly divided into three groups (n = 5). Mice in groups 1, 2, and 3 were injected with NDP-PEG-HAuNS, PEG-HAuNS, or saline control, respectively, and were treated with NIR laser as described in the proceeding section. Tumors were removed and cryosectioned for hematoxylin-eosin staining. The slices were examined under a Zeiss microscope. The images were taken using a Zeiss AxioCam MRc5 color camera, and the extent of tumor necrosis, expressed as a percentage of the entire tumor area, was analyzed with Zeiss AxioVision software (Version 4.6.3).

Statistical analysis

Comparisons of the number of green spots representing aggregates of HAuNS in tissue sections, tissue uptake of ^{111}In-labeled nanoparticles (%ID/g), [^{18}F]FDG uptake (%ID/g), and necrotic area as a percentage of tumor area were made using two-tailed Student's *t* test or

analysis of variance (for all groups). Differences between groups were considered statistically significant if P < 0.05.

3. Results and Discussions

Synthesis and characterization of NDP-MSH-PEG-HAuNS

NDP-MSH was conjugated to HAuNS through a PEG linker in the presence of excess of sulfohydryl methoxy-PEG (molecular weight, 5000; molar ratio NDP-MSH-PEG to PEG, 1:10). A small-molecular-weight peptide, $[Nle^4, D\text{-}Phe^7]\alpha$-MSH (NDP-MSH; molecular weight, 1604), was used as the homing ligand and was attached at the end of the PEG chains to ensure that the homing moieties were accessible to plasma membrane receptors and that the overall size of bioconjugated HAuNS remained at sub-nanometer level (Fig. 1A).

TEM depicted the NDP-MSH-PEG-HAuNS having a mean diameter of 43.5 ± 2.3 nm and mean shell thickness of 3–4 nm (Fig. 1B). The resonance absorbance of these nanoparticles was tuned to peak at 808 nm to match the center wavelength of the laser (Fig. 1C). Exposure of an aqueous solution of PEGylated HAuNS (7.3×10^{10} nanospheres/mL) to NIR laser light (808 nm, 8 W/cm^2) for 4 min elevated the temperatures of the solution from 25°C to 41.5°C ($\Delta T = 16.5$°C) (Supplementary Information, Fig. S3). The same level of temperature change was achieved with an aqueous solution of superparamagnetic iron oxide (SPIO)-silica cored gold nanospheres under the same experimental conditions, but with about 100 times higher nanoshell concentration (7.5×10^{12}) (9). The higher photothermal coupling efficiency of HAuNS compared with SPIO-silica cored gold nanoshells may be attributed to the excellent colloidal stability of PEGylated HAuNS (Fig. S4). The SPIO-silica cored gold nanoshells, on the other hand, formed aggregates in aqueous solution (9). The presence of such aggregates can decrease the amplitude of the plasmon resonance absorbance (28,29). Our data indicate that PEGylated HAuNS acted as an efficient photothermal coupling agent.

The presence of biologically active peptides in NDP-MSH-PEG-HAuNS was confirmed by immunogold staining (Fig. 1D).

Intracellular trafficking and in vitro photothermal ablation of melanoma cells

In order to track the internalization of NDP-MSH-PEG-HAuNS, fluorescein was conjugated to HAuNS using a fluorescein isothiocyanate (FITC) analogue containing lipoic acid (excitation/emission: 492/520 nm) (Supplementary Information, Fig. S2). Fluorescence images confirmed the presence of FITC-labeled NDP-MSH-PEG-HAuNS, but not FITC-labeled PEG-HAuNS, in the cytoplasm of B16/F10 melanoma cells (Fig. 2A). Moreover, co-incubation of B16/F10 cells with FITC-tagged NDP-MSH-PEG-HAuNS and a large excess of free NDP-MSH peptide blocked the cellular uptake of NDP-MSH-PEG-HAuNS, suggesting that NDP-MSH-conjugated HAuNS were taken up by cells via MC1R-mediated endocytosis (Fig. 2A). Since MC1R is a member of the G-protein-coupled receptor superfamily and since β-arrestins serve as adapters to link the activated G-protein-coupled receptors to the downstream cellular trafficking machinery (clathrin, AP-2 complexes) (30), we studied the possible role of β-arrestins in internalization of NDP-MSH-PEG-HAuNS. Fifteen minutes after treatment with FITC-tagged NDP-MSH-PEG-HAuNS, the distribution of β-arrestins displayed polarized fashion, which colocalized with NDP-MSH-PEG-HAuNS. In contrast, β-arrestins were uniformly distributed in the cytosol of M16/F10 melanoma cells incubated with PEG-HAuNS (Fig. 2B). These results suggested that internalization of NDP-MSH-PEG-HAuNS upon binding to MC1R involved recruitment of β-arrestins and that NDP-MSH-PEG-HAuNS acted as agonists for MC1R (31). As revealed by TEM, NDP-MSH-PEG-HAuNS and their aggregates were found in coated pits (Fig. 2C, arrowheads) and coated vesicles (early endosomes, Fig. 2C, arrow), suggesting the involvement of clathrin-coated pits in the

endocytosis of NDP-MSH-PEG-HAuNS/MC1R/β-arrestins complex (32). Interestingly, some NDP-MSH-PEG-HAuNS were found in the cytoplasm (Fig. 2C).

We used two dyes to probe the cell viability after exposure to NIR laser. Calcein AM reports ubiquitous intracellular esterase activity, while EthD-1 is a cell impermeable dye that is used to probe cell membrane integrity. Twenty-four hours after NIR irradiation (32 W/cm^2, 3 min), most B16/F10 cells treated with NDP-MSH-PEG-HAuNS were stained red with EthD-1, and there was absence of green calcein AM staining in these cells (Fig. 3A). In comparison, only a small fraction of cells were stained red with EthD-1 after treatment with PEG-HAuNS followed by NIR laser. The other control treatment groups (NIR alone, NDP-MSH-PEG-HAuNS alone) showed no observable damage to the cancer cells. At higher magnification, most of the cells treated with PEG-HAuNS plus NIR laser were polygonal (Fig. 3B, upper row) with few cells stained red with EthD-1. However, after treatment with NDP-MSH-PEG-HAuNS plus NIR laser, cell membranes were lysed and cell nuclei condensed (Fig. 3B, lower row, arrows). These results indicate that NDP-MSH-PEG-HAuNS mediated selective photothermal destruction of melanoma cells.

Previous studies showed that the threshold temperature in the range of 70–80°C was required for the destruction of tumor cells with the used of gold nanoparticles (33). Thermally-induced cellular injury/death above 40°C resulted from protein denaturation (34). There are two general effects of protein denaturation that one would expect to be particularly harmful to cells: direct inactivation of protein function and disruption of complex structures (35). Inactivation of enzyme activity, membrane receptors, and ion transporters has been shown to occur during hyperthermia (36). This can consist of membrane permeability changes, depolymerization of complex structures (e.g. disruption of cytoskeletal elements), and aggregation (e.g. aggregation of membrane proteins and binding of proteins to the nuclear matrix and other cytoskeletal structures). At higher temperature (i.e., 85–90°C), DNA and RNA also denature or unfold (34). In our study, the negative staining of calcein AM in B16/F10 melanoma cells treated with NDP-MSH-PEG-HAuNS plus NIR laser indicated the complete lost of ubiquitous intracellular esterase activity. A positive staining with EthD-1 in cells treated with the targeted HAuNS and laser indicated the disruption of cell membrane. Both inactivation of enzyme activity and disruption of cell membrane permeability could be attributed to the protein denaturation induced by photothermal effect. Further studies will be needed to investigate the temperature change in real-time during NIR laser irradiation, and protein denaturation and DNA unfolding transitions in relation to the observed temperature profile in order to clarify the mechanism of PTA mediated by HAuNS.

In vivo targeting to murine melanoma

Figure 4 compares distribution of NDP-MSH-PEG-HAuNS and PEG-HAuNS in MC1R-positive B16/F10 tumors grown subcutaneously in nude mice. Significantly higher uptake of FITC-tagged NDP-MSH-PEG-HAuNS than of FITC-tagged PEG-HAuNS in the tumor 4 h after intravenous injection of nanoparticles was observed. While PEG-HAuNS were scattered adjacent to the tumor vasculature, NDP-MSH-PEG-HAuNS were found throughout the tumor matrix, including in areas that were greater than 200 μm away from the nearest blood vessels (Fig. 4A). The distributions of both FITC-tagged NDP-MSH-PEG-HAuNS and FITC-tagged PEG-HAuNS in the other major organs are presented in Fig. 4B and Fig. S5. For NDP-MSH-PEG-HAuNS, the relative fluorescence intensity in different tissues was in the order of tumor > spleen > liver ≪ lung kidney > heart≈brain. For PEG-HAuNS, the order was spleen > liver ≪ tumor≈lung≈kidney≈heart≈brain (Fig. S5). It is important to note that more NDP-MSH-PEG-HAuNS were taken up by the tumors than by the liver and the spleen at 4 h after injection. Uptakes of both HAuNS in the liver and the spleen were primarily mediated by macrophages,

as confirmed by co-localization of HAuNS with macrophages stained positively for CD68 (Fig. S6).

For accurate quantitative analysis, HAuNS were further labeled with the γ emitter ^{111}In, which has a desirable decay half-life (t$_{1/2}$ = 67.3 h). Radiolabeling was accomplished through incubation of ^{111}InCl$_3$ with HAuNS tagged with the chelate agent, DTPA-TA. ITLC analysis showed that the radiochemical purities of NDP-MSH-PEG-HAuNS(DTPA-^{111}In) and PEG-HAuNS(DTPA-^{111}In) were greater than 99% (Fig. S7). After incubation in full mouse serum for 24 h, the radiochemical purity of both NDP-MSH-PEG-HAuNS(DTPA-^{111}In) and PEG-HAuNS(DTPA-^{111}In) remained greater than 95% (Fig. S7), indicating that the radiolabel on HAuNS was stable.

Biodistribution data obtained at 4 h after i.v. injection of radiolabeled HAuNS are summarized in Fig. 4C. The results confirmed significantly higher uptake of NDP-MSH-PEG-HAuNS (DTPA-^{111}In) in the tumor than that of PEG-HAuNS(DTPA-^{111}In) (12.6 ± 3.1%ID/g versus 4.3 ± 1.2%ID/g). In agreement with the results obtained by counting the particle clusters in tissue slices, mice injected with NDP-MSH-PEG-HAuNS(DTPA-^{111}In) showed the highest uptake in the tumor. Kidney, liver, lung, and spleen were other major organs taken up significant amount of HAuNS, but there was no significant difference between the group injected with NDP-MSH-PEG-HAuNS(DTPA-^{111}In) and the control group injected with non-targeted PEG-HAuNS(DTPA-^{111}In) in these organs. It is noted that the radioactivity of both nanoparticles in the blood pool was relatively high at 4 h after injection, suggesting the long blood half-lives of PEGylated HAuNS. The tumor-to-blood uptake ratio of NDP-MSH-PEG-HAuNS(DTPA-^{111}In) was about 1.0, while that of PEG-HAuNS(DTPA-^{111}In) was only 0.37.

Potential mechanisms for increasing nanoparticle delivery and dispersion in the tumor include increase in extravasation and interstitial transport (37). The observed transvascular distribution of PEG-HAuNS can be attributed to passive accumulation (18,20). However, the tumor-to-blood uptake ratio of non-targeted PEG-HAuNS was much lower than 1, suggesting that the EPR effect was not significant at the time of analysis (i.e., 4 h after injection). We believe that an active transport mechanism, operating through receptor-mediated endocytosis, is responsible for enhanced extravasation and dispersion of NDP-MSH-PEG-HAuNS into the tumor matrix. Our assertion is supported by the fact that the tumor-to-blood ratio of NDP-MSH-PEG-HAuNS(DTPA-^{111}In) was 2.7-fold higher than of PEG-HAuNS(DTPA-^{111}In). This assertion is further substantiated by Z-stack images of tumor sections at higher magnification, which revealed colocalization of NDP-MSH-PEG-HAuNS but not PEG-HAuNS with MC1R (Fig. 4D, arrowheads, yellow and orange colors resulting from overlapping green and red colors), confirming MC1R-mediated endocytosis of NDP-MSH-PEG-HAuNS *in vivo*.

Our results raise a number of interesting questions that must be further addressed. For example, what is the role of particle size in successful active targeting? We believe that HAuNS used in this study are ideally suited for targeted delivery not only because they are sufficiently small to pass through the pores of tumor vessels, but also because intracellular uptake of gold nanoparticles by mammalian cells is optimal when particle size is around 50 nm (38). In our recent work with HAuNS coated with monoclonal antibodies, only a moderate, albeit statistically insignificant increase in tumor uptake of antibody coated HAuNS was observed (17). It is reasonable to speculate that the much smaller size of peptide as compared to antibody used as the targeting moiety is responsible for successful active targeting demonstrated in the current work. Another question is related to the role of receptor-mediated endocytosis in extravasation and interstitial transport of NDP-MSH-PEG-HAuNS. The fact that NDP-MSH-PEG-HAuNS were rapidly transported to extravascular fluid space as far as 200 μm beyond the nearest microvessels can hardly be explained by a simple diffusion mechanism. Clearly,

further work is needed to elucidate the role of diffusion and/or transcytosis in enhancing extravasation and interstitial transport of targeted HAuNS in B16/F10 melanoma.

In vivo photothermal ablation of murine melanoma

Having shown that NDP-MSH-PEG-HAuNS were selectively delivered to B16/F10 melanoma, we next asked whether targeted delivery of NDP-MSH-PEG-HAuNS could translate into selective PTA of melanoma *in vivo*. We used [^{18}F]FDG PET to assess changes in metabolic activity after PTA. In mice injected with NDP-MSH-PEG-HAuNS, micro-PET showed markedly reduced tumor [^{18}F]FDG uptake 24 h after NIR treatment; the percentage of injected dose per gram of tumor (%ID/g) decreased by 86% (p = 0.0088) compared with the pretreatment value (Fig. 5A). In contrast, in mice injected with PEG-HAuNS or saline, tumor [^{18}F]FDG uptake was similar before and after NIR laser treatment. Moreover, tumor [^{18}F]FDG uptake was similar for tumors inoculated at contralateral sites not irradiated with NIR laser, indicating that reduced metabolic activity of tumors treated with NDP-MSH-PEG-HAuNS plus laser was not caused by NDP-MSH-PEG-HAuNS alone (Fig. 5A).

Histological examination confirmed that NDP-MSH-PEG-HAuNS plus laser caused significantly greater necrotic response than did PEG-HAuNS plus laser, saline plus laser, or saline only (Fig. 5B). About 66% of tissues were necrotized, characterized as pyknosis, karyolysis, cytoplasmic acidophilia, and degradation and corruption of the extracellular matrix of the tumor (Fig. 5B). Only a small fraction of necrotic tissues was found in the tumors treated with PEG-HAuNS plus NIR laser (7.9%). Thus, selective photothermal destruction of the target tumors mediated by NDP-MSH-PEG-HAuNS was confirmed both histologically (using excised tissue), and functionally ([^{18}F]FDG PET imaging). Early effects on metabolic activity as assesses by noninvasive [^{18}F]FDG PET imaging can be useful in monitoring response to PTA therapy. Long-term studies to evaluate the antitumor activity of targeted HAuNS in combination with NIR laser irradiation will need to be carried out to further confirm the short-term results obtained in the current studies.

The use of targeted HAuNS as photothermal coupling agents is particularly attractive in PTA of melanomas. Clinic data for the treatment of choroidal melanoma with an 810 nm-light used an output power of at least 300 mW for 1 min (3.0-mm spot in diameter), corresponding to a dose of ~255 J/cm^2 (4). In another study in a murine cutaneous melanoma model similar to the one used in the current study, a light dose of 1000 J/cm^2 was applied with a Nd:Yttrium-Lanthanum-Fluoride laser at 1047 nm (2). In our PTA experiment, subcutaneous murine melanoma in mice injected with targeted HAuNS was exposed to NIR light centered at 808 nm for 1 min at an output power of 0.5 W/cm^2, which corresponded to a light dose of 30 J/cm^2. Reduced laser power is highly desirable in order to avoid unnecessary damage to surrounding normal tissues. Finally, HAuNS contains nothing else other than pure gold. This is advantageous compared to other metal core/shell nanostructures that contain such materials as silica in the core (7–9). Colloidal gold has been safely used to treat rheumatoid arthritis for decades (39,40). Gold colloids have little toxicity or other adverse effects *in vivo* (41,42). Nevertheless, the long-term fate of HAuNS (as with other nanoparticles) after systemic injection requires further investigation.

4. Conclusions

Our current work establishes targeted HAuNS for *in vivo* PTA. The combination of spherical shape, small size (average diameter ~40 nm), absence of silica core, and tunable and strong absorption bands in NIR region makes these HAuNS ideally suited for PTA applications. By using a small-molecular-weight peptide as a targeting ligand and attaching it at the end of PEG chains, we demonstrated, for the first time, receptor-mediated active targeting of melanoma and efficient PTA with photothermal coupling agents *in vivo*. We further showed that

noninvasive [^{18}F]FDG PET can be useful in monitoring early treatment response after PTA. This can have significant implication in the clinic in guiding repeat ablation procedures.

Although our current study has shown promising results in selective PTA of melanoma using targeted HAuNS, much work remains to be done to advance this technology further into the clinic. For example, more detailed preclinical studies with regard to excretion/clearance, safety, and efficacy of targeted HAuNS need be documented. The physicochemical properties of HAuNS (including paricle size and surface characteristics) may be further improved to minimize their retention in the liver, the spleen, and the kidney. Studies correlating intratumoral distribution of HAuNS, temperature map, and thermal damage *in vivo* using noninvasive imaging techniques will be another area warrant future investigations.

Supplementary Material

Refer to Web version on PubMed Central for supplementary material.

Acknowledgments

References

1. Thompson JF, Scolyer RA, Kefford RF. Cutaneous melanoma. Lancet 2005;365:687–701. [PubMed: 15721476]

2. Dees C, Harkins J, Petersen MG, Fisher WG, Wachter EA. Treatment of murine cutaneous melanoma with near infrared light. Photochem Photobiol 2002;75:296–301. [PubMed: 11950096]

3. Shields CL, Shields JA, Cater J, et al. Transpupillary thermotherapy for choroidal melanoma: tumor control and visual results in 100 consecutive cases. Ophthalmol 1998;105:581–90.

4. Shields CL, Shields JA, DePotter P, Kheterpal S. Transpupillary thermotherapy in the management of choroidal melanoma. Ophthalmol 1996;103:1642–50.

5. Camerin M, Rello S, Villanueva A, et al. Photothermal sensitisation as a novel therapeutic approach for tumours: studies at the cellular and animal level. Eur J Cancer 2005;41:1203–12. [PubMed: 15911245]

6. Busetti A, Soncin M, Reddi E, Rodgers MA, Kenney ME, Jori G. Photothermal sensitization of amelanotic melanoma cells by Ni(II)-octabutoxy-naphthalocyanine. J Photochem Photobiol B 1999;53:103–9. [PubMed: 10672535]

7. Hirsch LR, Stafford RJ, Bankson JA, et al. Nanoshell-mediated near-infrared thermal therapy of tumors under magnetic resonance guidance. Proc Natl Acad Sci U S A 2003;100:13549–54. [PubMed: 14597719]

8. Gobin AM, Lee MH, Halas NJ, et al. Near-infrared resonant nanoshells for combined optical imaging and photothermal cancer therapy. Nano Lett 2007;7:1929–34. [PubMed: 17550297]

9. Ji X, Shao R, Elliott AM, et al. Bifunctional gold nanoshells with a superparamagnetic iron oxide-silica core suitable for both MR imaging and photothermal therapy. J Phys Chem C 2007;111:6245–51.

10. Skrabalak SE, Au L, Lu X, Li X, Xia Y. Gold nanocages for cancer detection and treatment. Nanomed 2007;2:657–68. [PubMed: 17976028]

11. Huang X, El-Sayed IH, Qian W, El-Sayed MA. Cancer cells assemble and align gold nanorods conjugated to antibodies to produce highly enhanced, sharp, and polarized surface Raman spectra: a potential cancer diagnostic marker. Nano Lett 2007;7:1591–7. [PubMed: 17474783]

12. Loo C, Lin A, Hirsch L, et al. Nanoshell-enabled photonics-based imaging and therapy of cancer. Technol Cancer Res Treat 2004;3:33–40. [PubMed: 14750891]

13. O'Neal DP, Hirsch LR, Halas NJ, Payne JD, West JL. Photo-thermal tumor ablation in mice using near infrared-absorbing nanoparticles. Cancer Lett 2004;209:171–6. [PubMed: 15159019]

14. Qian X, Peng XH, Ansari DO, et al. In vivo tumor targeting and spectroscopic detection with surface-enhanced Raman nanoparticle tags. Nat Biotechnol 2008;26:83–90. [PubMed: 18157119]

15. Liu Z, Cai W, He L, et al. In vivo biodistribution and highly efficient tumour targeting of carbon nanotubes in mice. Nat Nanotechnol 2007;2:47–52. [PubMed: 18654207]

16. Schwartzberg AM, Olson TY, Talley CE, Zhang JZ. Synthesis, characterization, and tunable optical properties of hollow gold nanospheres. J Phys Chem B 2006;110:19935–44. [PubMed: 17020380]

17. Melancon MP, Lu W, Yang Z, et al. In vitro and in vivo targeting of hollow gold nanoshells directed at EGF receptors. Mol Cancer Ther 2008;7:1730–9. [PubMed: 18566244]

18. Brigger I, Dubernet C, Couvreur P. Nanoparticles in cancer therapy and diagnosis. Adv Drug Deliv Rev 2002;54:631–51. [PubMed: 12204596]

19. Arrueboa M, Fernández-Pachecoa R, Ibarraa RM, Santamaríaa J. Magnetic nanoparticles for drug delivery. Nanotoday 2007;2:22–32.

20. Moghimi SM, Hunter AC, Murray JC. Long-circulating and target-specific nanoparticles: theory to practice. Pharmacol Rev 2001;53:283–318. [PubMed: 11356986]

21. Hobbs SK, Monsky WL, Yuan F, et al. Regulation of transport pathways in tumor vessels: role of tumor type and microenvironment. Proc Natl Acad Sci U S A 1998;95:4607–12. [PubMed: 9539785]

22. Kong G, Braun RD, Dewhirst MW. Hyperthermia enables tumor-specific nanoparticle delivery: effect of particle size. Cancer Res 2000;60:4440–5. [PubMed: 10969790]

23. Giblin MF, Wang N, Hoffman TJ, Jurisson SS, Quinn TP. Design and characterization of alpha-melanotropin peptide analogs cyclized through rhenium and technetium metal coordination. Proc Natl Acad Sci U S A 1998;95:12814–8. [PubMed: 9788997]

24. Miao Y, Benwell K, Quinn TP. ^{99m}Tc- and ^{111}In-labeled alpha-melanocyte-stimulating hormone peptides as imaging probes for primary and pulmonary metastatic melanoma detection. J Nucl Med 2007;48:73–80. [PubMed: 17204701]

25. Siegrist W, Solca F, Stutz S, et al. Characterization of receptors for alpha-melanocyte-stimulating hormone on human melanoma cells. Cancer Res 1989;49:6352–8. [PubMed: 2804981]

26. Sawyer TK, Sanfilippo PJ, Hruby VJ, et al. 4-Norleucine, 7-D-phenylalanine-alpha-melanocyte-stimulating hormone: a highly potent alpha-melanotropin with ultralong biological activity. Proc Natl Acad Sci U S A 1980;77:5754–8. [PubMed: 6777774]

27. Chen J, Cheng Z, Hoffman TJ, Jurisson SS, Quinn TP. Melanoma-targeting properties of (99m) technetium-labeled cyclic alpha-melanocyte-stimulating hormone peptide analogues. Cancer Res 2000;60:5649–58. [PubMed: 11059756]

28. Hirsch LR, Gobin AM, Lowery AR, et al. Metal nanoshells. Ann Biomed Eng 2006;34:15–22. [PubMed: 16528617]

29. Quinten M. The color of finely dispersed nanoparticles. Appl Phys B 2001;73:317–326.

30. Shenoy SK, Lefkowitz RJ. Multifaceted roles of beta-arrestins in the regulation of seven-membrane-spanning receptor trafficking and signalling. Biochem J 2003;375:503–15. [PubMed: 12959637]

31. Cai M, Stankova M, Pond SJK, et al. Real Time Differentiation of G-Protein Coupled Receptor (GPCR) Agonist and Antagonist by Two Photon Fluorescence Laser Microscopy. J Am Chem Soc 2004;126:7160–1. [PubMed: 15186137]

32. Claing A, Laporte SA, Caron MG, Lefkowitz RJ. Endocytosis of G protein-coupled receptors: roles of G protein-coupled receptor kinases and beta-arrestin proteins. Prog Neurobiol 2002;66:61–79. [PubMed: 11900882]

33. Huang X, Jain PK, El-Sayed IH, El-Sayed MA. Determination of the minimum temperature required for selective photothermal destruction of cancer cells with the use of immunotargeted gold nanoparticles. Photochem Photobiol 2006;82:412–7. [PubMed: 16613493]

34. He X, Wolkers W, Crowe JH, Bischof JC. In situ thermal denaturation of proteins in Dunning AT-1 prostate cancer cells: implication for hyperthermic cell injury. Ann Biomed Eng 2004;32:1384–98. [PubMed: 15535056]

35. Lepock JR. Cellular effects of hyperthermia: relevance to the minimum dose for thermal damage. Int J Hyperthermia 2003;19:252–66. [PubMed: 12745971]

36. Laszlo A. The effects of hyperthermia on mammalian cell structure and function. Cell Prolif 1992;25:59–87. [PubMed: 1554820]

37. Lu D, Wientjes MG, Lu Z, Au JL. Tumor priming enhances delivery and efficacy of nanomedicines. J Pharmacol Exp Ther 2007;322:80–8. [PubMed: 17420296]

38. Chithrani BD, Ghazani AA, Chan WC. Determining the size and shape dependence of gold nanoparticle uptake into mammalian cells. Nano Lett 2006;6:662–8. [PubMed: 16608261]

39. Makin M, Robin GC. Chronic synovial effusions treated with intra-articular radioactive gold. JAMA 1964;188:725–8. [PubMed: 14122679]

40. Boerbooms AM, Buijs WC, Danen M, van de Putte LB, Vandenbroucke JP. Radio-synovectomy in chronic synovitis of the knee joint in patients with rheumatoid arthritis. Eur J Nucl Med 1985;10:446–9. [PubMed: 2988961]

41. Connor EE, Mwamuka J, Gole A, Murphy CJ, Wyatt MD. Gold nanoparticles are taken up by human cells but do not cause acute cytotoxicity. Small 2005;1:325–7. [PubMed: 17193451]

42. Shukla R, Bansal V, Chaudhary M, et al. Biocompatibility of gold nanoparticles and their endocytotic fate inside the cellular compartment: a microscopic overview. Langmuir 2005;21:10644–54. [PubMed: 16262332]

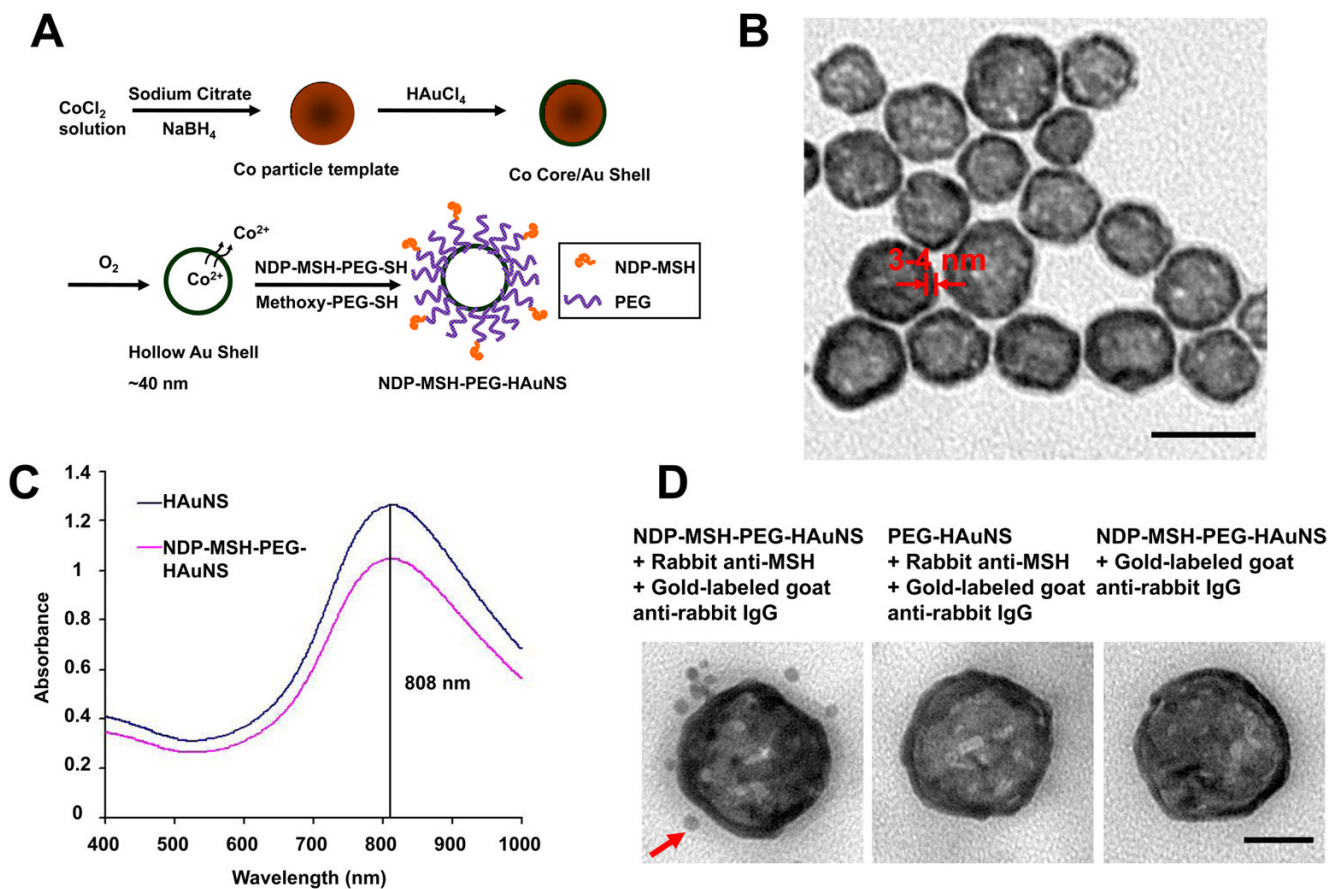**Fig. 1.**
Conjugation of NDP-MSH peptide to HAuNS through PEG linker. *A*, Schematic of nanoshell synthesis and bioconjugation. *B*, TEM image of NDP-MSH-PEG-HAuNS. Bar = 50 nm. *C*, Absorbance of HAuNS in water before and after bioconjugation. *D*, TEM images of NDP-MSH-PEG-HAuNS and PEG-HAuNS subjected to immunogold staining. Only NDP-MSH-PEG-HAuNS were stained with 5-nm gold nanoparticles (arrow). Bar = 20 nm.
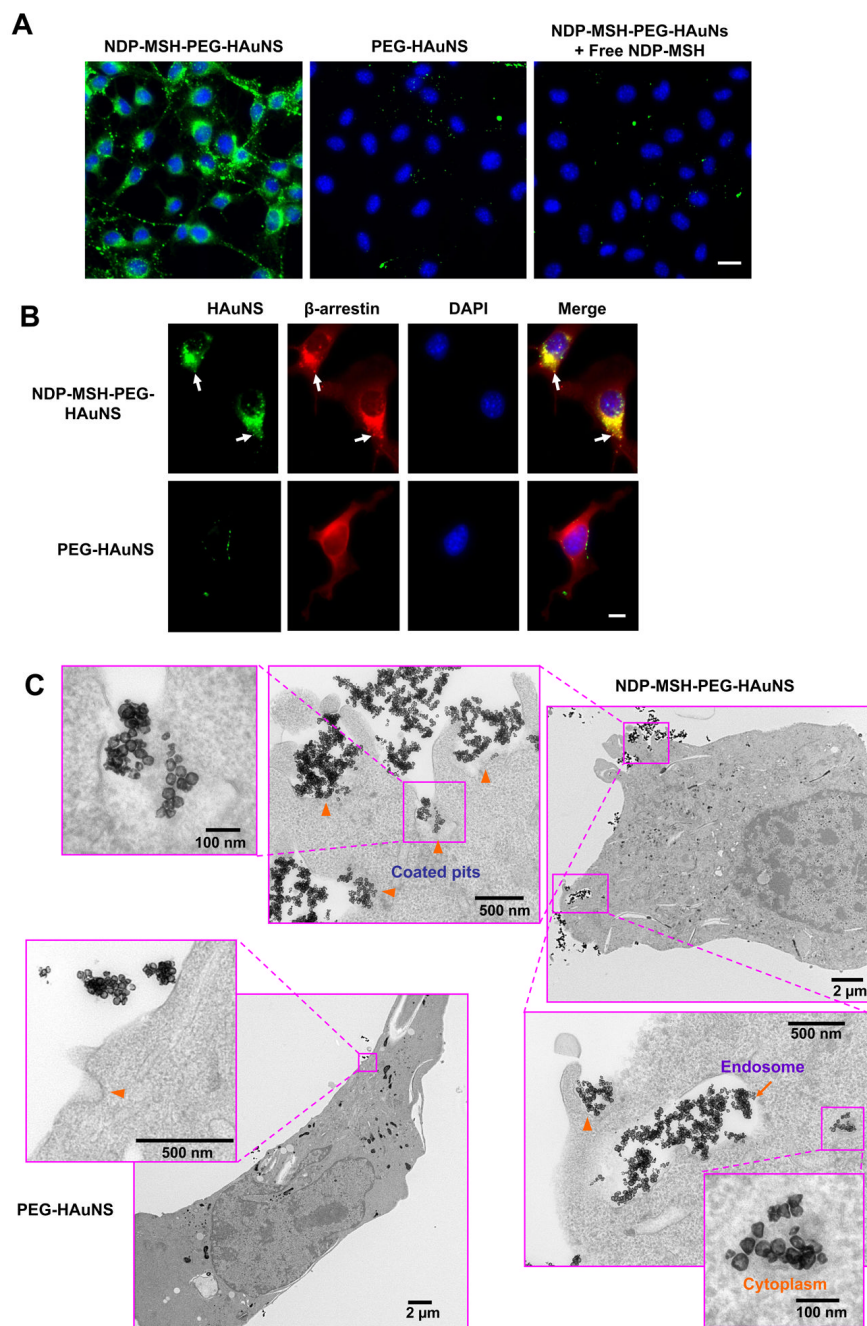
Fig. 2.
Specific uptake of NDP-MSH-PEG-HAuNS in B16/F10 cells. *A*, Uptake of FITC-tagged HAuNS in B16/F10 cells. Cell nuclei were counterstained with DAPI (blue). Bar = 20 μm. *B*, Distribution of β-arrestin expression in relation to FITC-tagged HAuNS in B16/F10 cells. In cells incubated with NDP-MSH-PEG-HAuNS, the HAuNS (green) colocalized with β-arrestin (red) in polarized fashion (yellow, arrows), whereas in cells incubated with PEG-HAuNS, β-arrestin was evenly distributed in the cytoplasm and did not colocalize with the HAuNS. Cell nuclei were counterstained with DAPI (blue). Bar = 10 μm. *C*, TEM images of B16/F10 cells incubated with NDP-MSH-PEG-HAuNS or PEG-HAuNS. The electron-dense

NDP-MSH-PEG-HAuNS were seen in coated pits (arrowheads), early endosomes (arrow), and cytoplasm. PEG-HAuNS were found only outside the cell membrane.
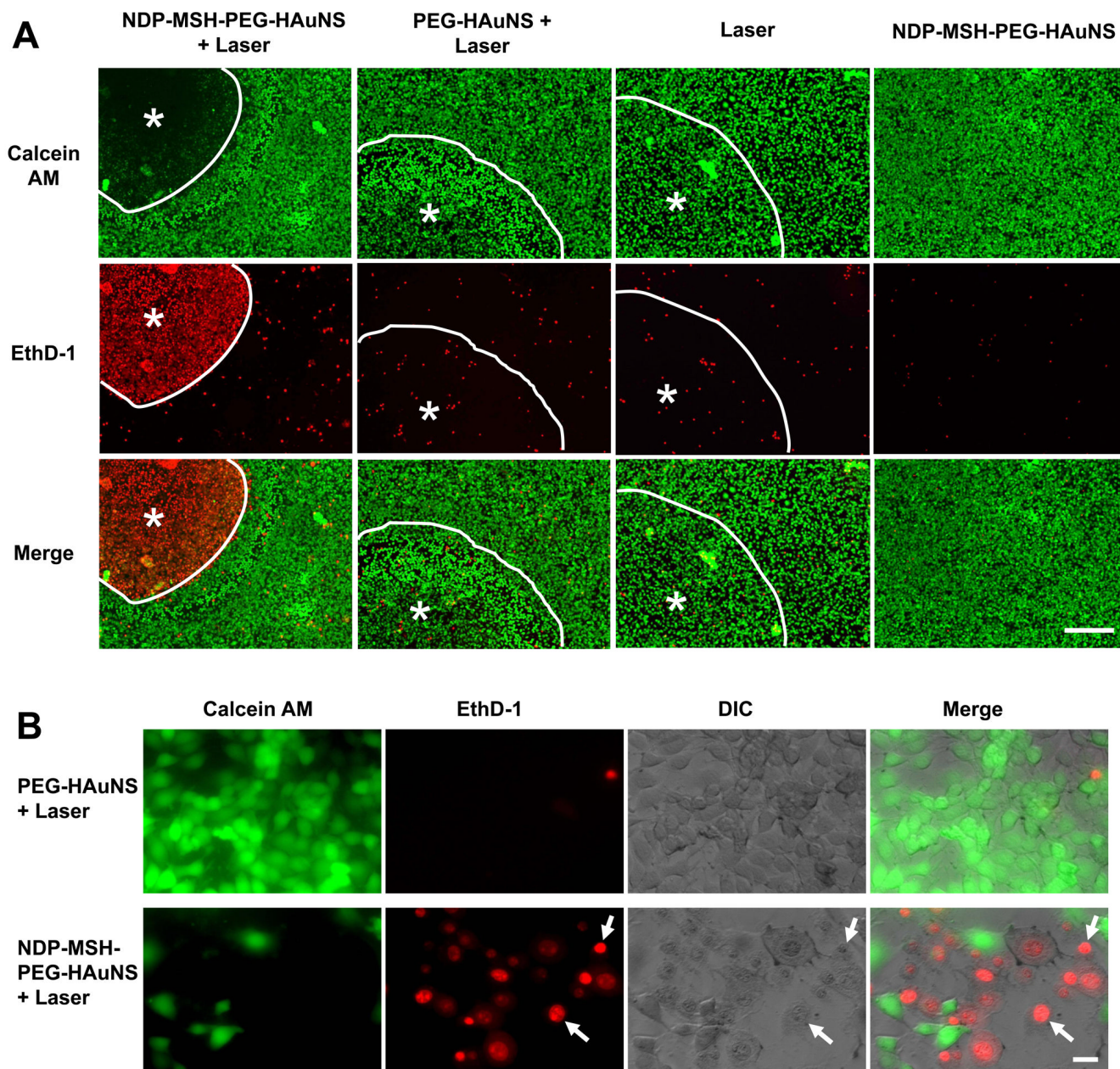
Fig. 3.
Cell viability after NIR irradiation. B16/F10 cells were treated with different HAuNS and NIR light centered at 808 nm (32 W/cm^2, 3 min). *A*, After treatment with PEG-HAuNS plus NIR laser, NIR laser alone, or NDP-MSH-PEG-HAuNS alone, cells retained normal morphology, and few dead cells were observed. In contrast, after treatment with NDP-MSH-PEG-HAuNS plus NIR laser, most cells were dead. Viable cells were stained green with calcein AM, dead cells were stained red with EthD-1. Circled area labeled with asterisk represents laser-irradiated area. Bar = 100 μm. *B*, Microphotographs of cells treated with PEG-HAuNS plus NIR laser (upper panel) and NDP-MSH-PEG-HAuNS plus NIR laser (lower panel) at higher magnification. Cells treated with PEG-HAuNS plus NIR laser were viable and polygonal,

whereas most cells treated with NDP-MSH-PEG-HAuNS plus NIR laser were rounded and lost membrane integrity (arrows). DIC, differential interference contrast. Bar = 20 μm.

NIH-PA Author Manuscript

NIH-PA Author Manuscript

NIH-PA Author Manuscript
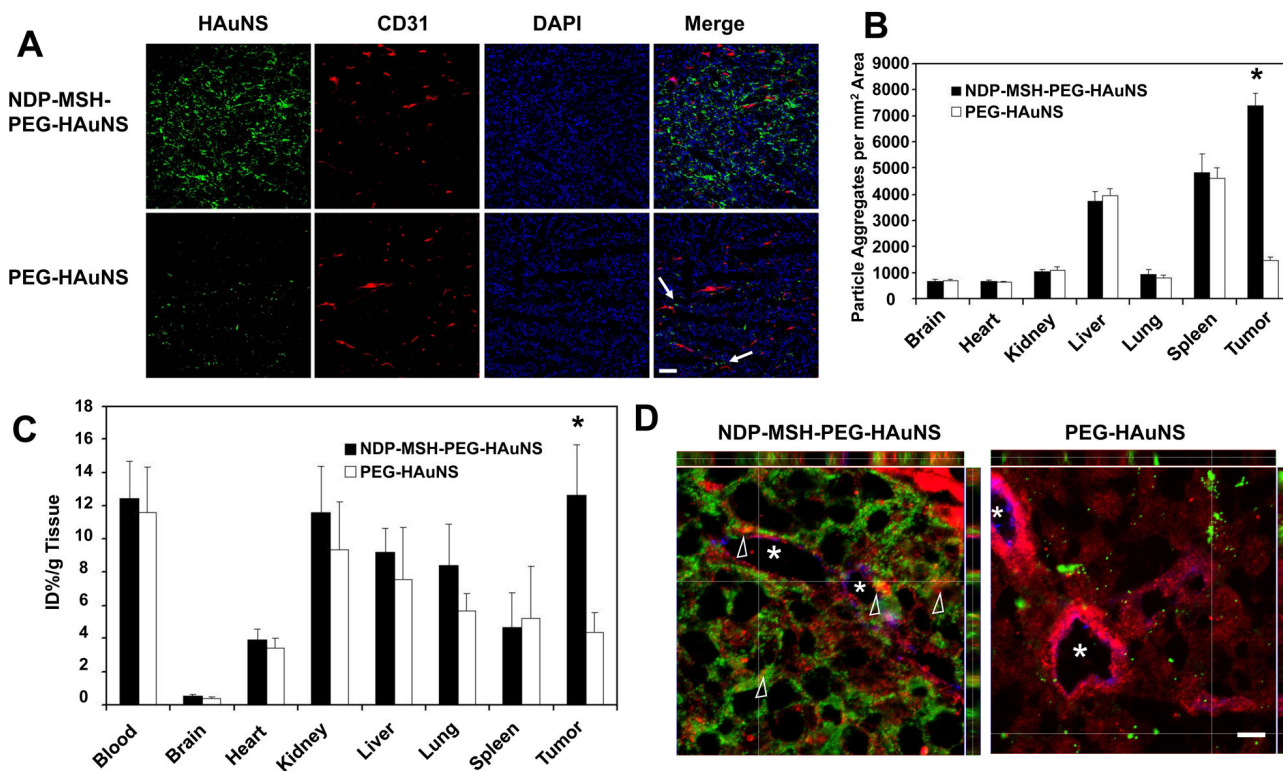
Fig. 4.
Biodistribution and intratumoral distribution of FITC-tagged HAuNS. Tissue and tumors were removed 4 h after intravenous injection of HAuNS. *A*, Representative fluorescence micrographs of cryosectioned B16/F10 melanoma. Microvessels (red) were stained with rat anti-mouse CD31 monoclonal antibody. Cell nuclei were counterstained with DAPI (blue). Significantly more HAuNS (green) were found in the tumors of mice injected with NDP-MSH-PEG-HAuNS than in the tumors of mice injected with PEG-HAuNS. NDP-MSH-PEG-HAuNS were distributed throughout the tumor matrix in the interstitial space, whereas PEG-HAuNS were distributed around tumor vessels (arrows). Bar = 100 μm. *B*, Biodistribution of FITC-tagged HAuNS in different tissues. Data were calculated as the number of particle aggregates per mm² visual area at ×200, and values are presented as mean ± SD (n = 5). Bars, SD. *P < 0.01. Microphotographs of FITC-tagged HAuNS in other major organs are shown in Fig. S5. *C*, Biodistribution of NDP-MSH-PEG-HAuNS(DTPA-^{111}In) and PEG-HAuNS (DTPA-^{111}In). Data were plotted as % injected dose per gram of tissue (% ID/g). Mean ± SD (n = 5). *P < 0.01. *D*, Z-stack images of tumor sections at higher magnification. MC1R was stained with rabbit anti-mouse MC1R polyclonal antibody (pseudocolored red). Blood vessels were stained with rat anti-mouse CD31 monoclonal antibody (pseudocolored blue). FITC-tagged HAuNS were green. NDP-MSH-PEG-HAuNS but not PEG-HAuNS colocalized with MC1R (yellow and orange, arrowheads), indicating MC1R-mediated endocytosis of NDP-MSH-PEG-HAuNS *in vivo*. Asterisks indicate the lumens of tumor vasculature with discontinuous CD31 staining. Bar = 10 μm.
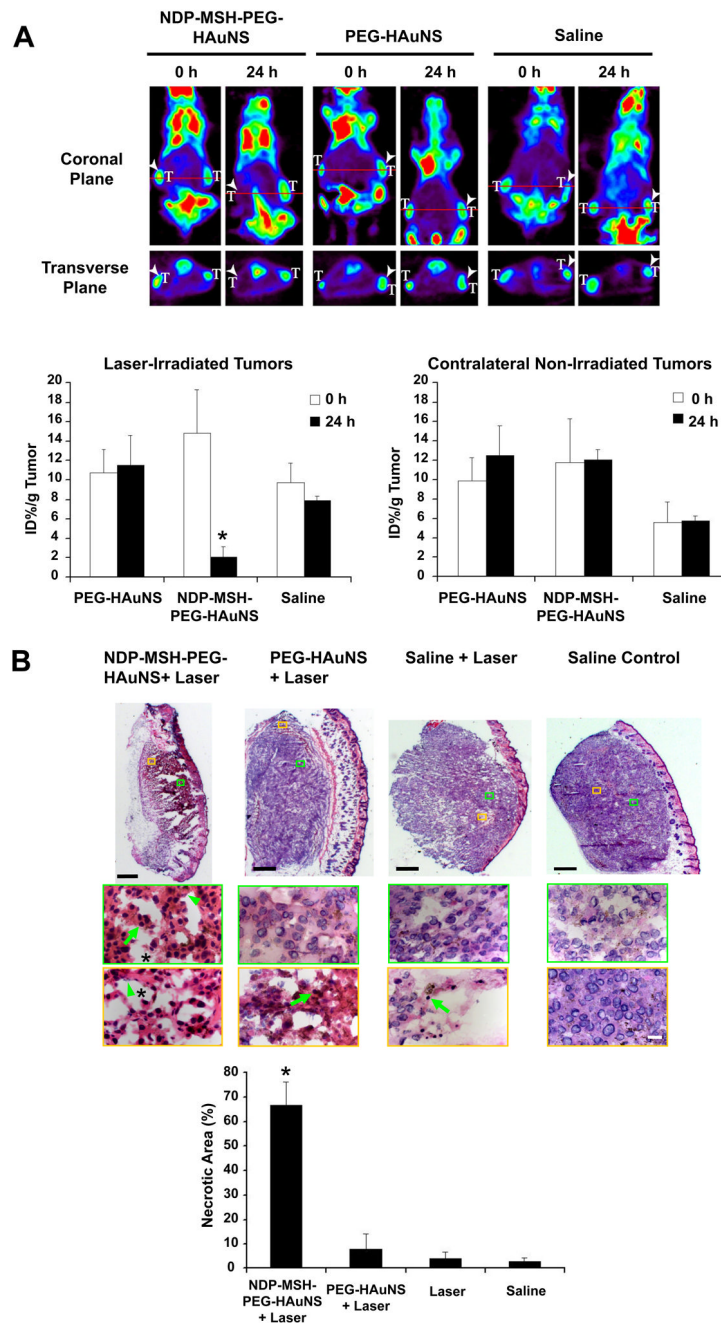
Fig. 5.
In vivo PTA with targeted NDP-MSH-PEG-HAuNS induced selective destruction of B16/F10 melanoma in nude mice. *A*, [18F]FDG PET imaging shows significantly reduced metabolic activity in tumors after PTA in mice pretreated with NDP-MSH-PEG-HAuNS but not in mice pretreated with PEG-HAuNS or saline. [18F]FDG PET was conducted before (0 h) and 24 h after NIR laser irradiation (0.5 W/cm^2 at 808 nm for 1 min), which was commenced 4 h after intravenous injection of HAuNS or saline. T: tumor. Arrowheads: tumors irradiated with NIR light. [18F]FDG uptakes (%ID/g) before and after laser treatment are shown graphically at the bottom. Bars, SD (n=3). *, $P < 0.01$ for %ID/g posttreatment versus %ID/g pretreatment. *B*, Histological assessment of tumor necrosis. Representative photographs of whole tumors

stained with hematoxylin-eosin 24 h after NIR irradiation. Bar =500 μm. Representative microphotographs at high magnification show tumor cells characterized by extensive pyknosis (arrows), karyolysis (arrowheads), cytoplasmic acidophilia, and degradation of the extracellular matrix of the tumor (asterisks) in mice treated with NDP-MSH-PEG-HAuNS plus laser. In mice treated with PEG-HAuNS plus laser, such features were observed mostly in areas close to the surface. Bar = 50 μm. The necrotic area as a percentage of the tumor is shown in the bar graph. *, $P < 0.05$. Bars, SD (n=5).